Authors' accepted manuscript
Article published in Applied Acoustics, Vol. 216, 2024.
The final published version available at https://doi.org/10.1016/j.apacoust.2023.109744

# Thin metamaterial using acoustic black hole profiles for broadband sound absorption.

Gauthier Bezançon[1], Olivier Doutres[1], Olga Umnova[2], Philippe Leclaire[3] and Thomas Dupont[1]

[1] *Department of Mechanical Engineering, École de Technologie Supérieure, Montréal, Québec, Canada*

[2] *University of Salford, Manchester, England, UK*

[3] *DRIVE – ISAT Université de Bourgogne, Nevers, France*

Corresponding author

E-mail address: gauthier.bezancon.1@ens.etsmtl.ca (G. Bezançon)



**Keywords**

- Sound absorbers
- Acoustic metamaterial
- Microstructure design
- Acoustic black hole
- Broadband absorption
- Complex frequency plane

**Abstract**

The multi-pancake absorber is a thin acoustic metamaterial composed of periodically arranged thin annular cavities separated by the plates and connected by a main pore, enabling low frequency

sound absorption. However, with a constant main pore radius, this structure exhibits tonal absorption behavior characterized by narrow peaks with varying amplitudes due to an imbalance in losses between the modes. This work investigates a geometric variation of the main pore, focusing on the designs with a gradually decreasing radius known as acoustic black hole profiles, to achieve broadband absorption. An analytical model based on the transfer matrix approach and lumped elements is proposed to predict the acoustic properties. Validation is conducted through thermo-visco-acoustic finite element simulations and impedance tube measurements. Multiple main pore profiles are investigated and the complex frequency plane representation is used to improve the balance of losses. An understanding of the influence of the main pore radius at the entrance and backing of the sample, allows design of a decreasing main pore radius profile that results in a high absorption coefficient value across a broad frequency range. Non-linear decreasing main pore profiles can be used, if necessary, to accentuate losses and achieve absorption peaks of similar amplitude.



## 1. Introduction

Acoustic absorbers are essential for managing and reducing noise in various environments including offices, concert halls, industrial facilities, or transportation. Porous and fibrous materials are commonly used as conventional passive treatments for noise control due to their effective acoustic absorption properties [1] [2]. In order to achieve efficient absorption in a particular frequency range, it is recommended to consider a hard-backed material slab with thickness that is greater than the quarter of the largest wavelength. This means that a substantial material thickness is required for effective broadband absorption especially at low frequencies. Moreover, the

flammability of most porous and fibrous materials renders them unsuitable for use in harsh environments like engines or reactors. Furthermore, certain types of foam can present hygiene and health risk as they release particles during use. Additionally, conventional reactive materials like simple resonators [3] [4] can absorb sound of various frequencies with an adequate cavity air volume, but they typically exhibit a single, narrow absorption peak.

In recent years, extensive research has been conducted on artificial materials designed to possess unusual acoustic properties, also known as acoustic metamaterials. They generally have periodic structure and are capable of interacting with sound waves in a controlled manner, allowing them to be used for absorption, transmission, and acoustic focusing. Liao et al. [5] have conducted a thorough literature review, offering a comprehensive survey and classification of the latest research advancements in the field of acoustic metamaterials. Numerous metamaterial structures, such as periodic arrays of quarter-wavelength resonators [6], Helmholtz resonators (HR) [7] [8], labyrinthine cavities [9], and honeycomb cells [10], have been investigated for acoustic absorption. These metamaterials employ configurations of individual cavities, where each absorption peak corresponds to the resonance of a specific cavity. The resonances of the cavities are therefore not (or weakly) coupled. This characteristic allows for precise control of the absorption peaks by manipulating the geometric parameters of the corresponding cavity. However, as a consequence, these metamaterials tend to be relatively thick, wide, or exhibit a small number of cavities, resulting in limited number of absorption peaks.

Leclaire et al. [11] have studied a metamaterial with a main perforation containing periodically spaced dead-end pores. At low frequencies, the presence of a periodic lattice of dead-end pores increases the effective compressibility of the metamaterial without modifying the effective dynamic density. This induces a decrease in the effective sound speed leading to the appearance

of multiple absorption peaks at low frequencies. Based on this work, Dupont et al. [12] have proposed a thin acoustic metamaterial, called multi-pancake absorber, with improved properties. This absorber is composed of periodically spaced identical annular plates separated by very thin annular cavities, also called “pancake cavities”. This metamaterial exhibits numerous coupled resonances. This design enables the development of materials only a few centimeters thick with several absorption peaks ranging from a few hundred hertz to several thousand hertz. Using an effective fluid model, Brooke et al. [13] have derived an analytical expression for the absorption peak value and the frequency of the first resonance of this metamaterial, relating them to the geometrical parameters of the structure. Kone et al. [14] have proposed a variation of this geometry with a non-centered main pore to improve low frequency absorption. However, multi-pancake absorbers have relatively narrow absorption peaks and not all of them with high peak values, which may be relevant for attenuation of tonal sounds but not for the broadband ones. Nevertheless, in the metamaterial proposed by Dupont et al. [12], the geometry of the main pore profile could be modified along the material thickness to improve the acoustic performance.

Sound absorbers with property gradients, such as acoustic black holes (ABH), have gained attention in the past few years. Mironov and Pislyakov [15] have studied a structure comprised a series of circular annular plates, periodically spaced with a main pore radius gradually decreasing from the front to the back of the sample. This geometry induces a progressive decrease of the wave speed through the structure leading to the reduction or even the suppression of the reflected acoustic waves. Later, El Ouahabi et al. [16] have experimentally studied ABH structures with a linearly and quadratically decreasing main pore profile. Deaconu et al. [17] have numerically studied different mufflers using ABH principle with various design. Using finite element simulations and experiments, Xiaoqi and Li [18] have proposed a structure combining ABH and

microperforated plates. Guasch et al. [19] have used a transfer matrix model to predict the reflection coefficient of an ABH composed of annular plates and cavities, but the matrix segmentation developed for large air cavities may not be suitable for very thin ABHs with thinner cavities. Then, Mironov and Pislyakov [20] proposed a continuous analytical model to calculate the acoustic properties of their ABH. More recently, Umnova et al. [21] have developed a semi-analytical equivalent fluid model for a material combining ABH features and losses in the lateral cavities and the main pore. They demonstrated that a high absorption coefficient value can be obtained for a wide range of frequencies. They studied in details the influence of the ABH overall thickness, as well as those of the cavities. The absorption at lower frequencies is due to resonances along the structure, called global resonances, while sound absorption at higher frequencies is due to resonances of the cavities, called local resonances. Additionally, it is shown that a thin resonant cavity behaves like a rigid wall beyond its resonance frequency. Thus, the high frequency limit of the absorption range is determined by the resonance frequency of the first cavity at the front of the material. This conclusion is in line with Mironov and Pislyakov [15] who considered only the frequencies below the resonances of the cavities. While materials with ABH profiles are effective for broadband absorption, they often contain numerous relatively large cavities (several millimeters wide) resulting in considerable overall thickness. Therefore, ABH profiles with the geometry of the metamaterial proposed by Dupont et al. [12] holds potential for creating a broadband material with very low thickness. Furthermore, investigating the global and local resonances, as well as sound propagation, in such a metamaterial, as was done by Umnova et al. [21], can enhance the understanding of its acoustic behavior. Moreover, this can provide insights into the frequency limitations of absorption by materials with similar main perforation profiles but

composed of fewer cells. Furthermore, a parametric analysis of the central perforation profile effect on the absorption coefficient would be useful for its improvement.

Various quantities were used to analyze acoustic metamaterials, such as the absorption coefficient, the wave speed along the material, or the pressure distribution at given frequencies. Romero-García et al. [22] proposed an approach based on the analysis of the complex frequency plane representation to achieve perfect absorption by manipulating the absorption peaks of a resonant material. The technique allows visualizing whether a mode has insufficient or excessive loss, thus making it possible to balance it for achieving perfect absorption at the corresponding absorption peak. Starting from a material composed of two HRs in series and visualizing the complex frequency plane representation to add additional resonators one by one, Jiménez et al. [23] have designed a rainbow-trapping absorbers with a perfect broadband sound absorption. The final panels were composed of a pseudo-periodic array of HRs with graded dimensions. The dimensions of each cell control the corresponding absorption peak, thus arranging them tightly together forms a frequency band of high absorption coefficient. However, this implies that the resonances are not (or weakly) coupled, which may not be an optimal use of the material volume. Nevertheless, this work highlights the usefulness of the complex frequency plane representation as a tool for analyzing the effect of losses on the local resonances in metamaterials and better understanding how to balance these losses to improve absorption.

This paper aims to improve the acoustic absorption of the thin multi-pancake metamaterial proposed by Dupont et al. [12] through the incorporation of an ABH main pore profile to achieve broadband absorption. In this metamaterial, the resonance modes are coupled with each other, resulting in reduced material volume. The global and local resonances are analyzed for understanding the acoustic behavior. Additionally, the complex frequency plan representation is

used to provides a distinctive approach for enhanced comprehension and design of this innovative multi-resonant structure.

The paper is organized as follows. In section 2, the metamaterial structure is described and an analytical model is developed based on a transfer matrix formulation and lumped elements for the annular cavities. Then, the numerical finite element model is presented and the manufacturing of the sample is detailed. The analytical model is then verified against numerical simulations and validated against measurements in section 3.1. As a first step, an analysis of a structure with a constant main pore profile is developed thanks to the complex frequency plane representation and presented in section 3.2. Subsequently, in section 3.3, the acoustic behavior of metamaterials with a decreasing or increasing main pore radius is described with regard to the local resonances of the thin cavities. Then, section 3.4 details a parametric analysis of ABH profiles based on the insights gained from the previous sections, for linear and non-linear decreasing profiles of the main pore radius. Finally, broadband ABHs are proposed and presented in section 3.5.



## 2. Material and methods

### 2.1. Material

The proposed metamaterial (see **Fig. 1**) is composed of $N = 15$ pseudo-periodic unit cells (PPUC), each consisting of a main pore and a thin cylindrical cavity called here "full cavity". The thickness of each main pore is $h_{mp} = 1$ mm and the thickness of each full cavity is $h_{cav} = 1$ mm. The total thickness of the material is therefore $L = 31$ mm, including the last plate which serves as a rigid termination. The overall geometry is cylindrical with a radius of $R_{samp} = 22.2$ mm. The external radius of all the cavities is $R_{cav} = 21$ mm. These geometrical parameters will remain

constant throughout this study and have been chosen to be consistent with the geometry previously investigated in a previous paper (see sample *B* in [12]).

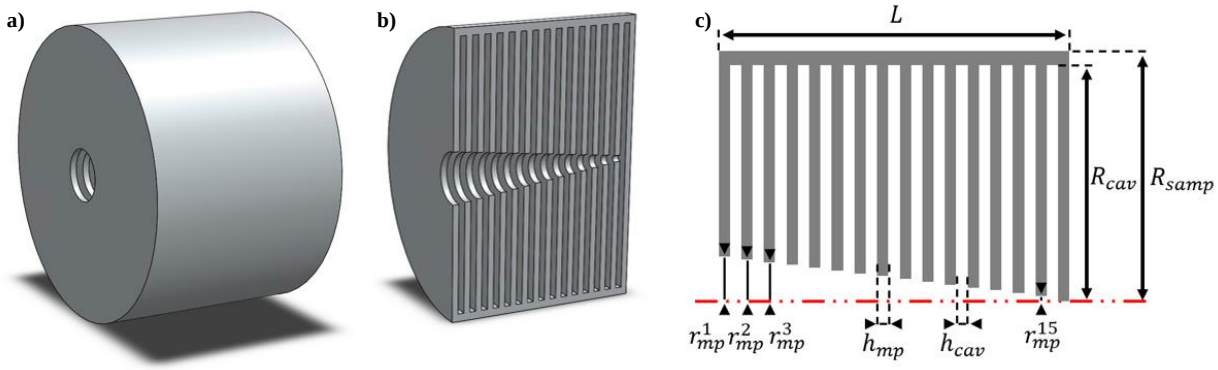


**Fig. 1.** Visualization of the proposed metamaterial: a) 3D global, b) 3D cross-sectional and c) 2D cross-sectional view of the metamaterial with a defined profile such as $r_{mp}^1 = 4$ mm, $r_{mp}^{15} = 0.5$ mm and $p = 1$.

The variable parameters in this work are limited to the 15 main pore radii $r_{mp}^i$ with $i$ ranging from 1 to $N = 15$, that can be controlled all at once through a profile function. To characterize continuous profiles along the material thickness, the radius of the $i^{th}$ main pore $r_{mp}^i$ is defined as a function of the radius of the first main pore $r_{mp}^1$, of the last main pore $r_{mp}^{15}$, and of a parameter $p$ that controls the rate of radius variations along the thickness of the material:

$$r_{mp}^i = r_{mp}^1 - \left(r_{mp}^1 - r_{mp}^{15}\right)\left(\frac{i-1}{N-1}\right)^p \quad (1)$$

Therefore, for a constant radius profile $p = 0$ and $r_{mp}^i = r_{mp}^1$ and for a linear profile $p = 1$.

### 2.2. Analytical Model

This section presents an analytical model developed using the transfer matrix formulation and lumped elements, called transfer matrix model (TMM) hereinafter. It is based on the model employed by Dupont et al. [12] but further adapted to account for non-constant profiles of the main pore. The adaptation of the model is thus mainly achieved by determining the characteristics of the common volumes (referred to as the "common pore" in [12]) as detailed in the following. The

metamaterial is divided into several layers which are each describe by a 2 by 2 matrix linking acoustic pressure and velocity on each side of the layer. The transfer matrix method is valid when the plane wave condition is satisfied which corresponds to f $<$ 4 200 Hz in a cylindrical tube with a radius of $R_{samp} = 22.2$ mm.

The material is composed of a succession of PPUC, each consisting of a main pore (subscript $mp$) and a full cavity (subscript $F\_cav$) represented by transfer matrices $\mathrm{T}_{mp}^{i}$ and $\mathrm{T}_{F\_cav}^{i}$. The transfer matrix of the material slab is given by:

$$\mathrm{T}_{mat} = \prod_{i=1}^{N} \mathrm{T}_{mp}^{i}\, \mathrm{T}_{F\_cav}^{i} \tag{2}$$

with $N = 15$ the number of PPUC.

The main pores are cylinders with thickness $\mathrm{h}_{mp}$ and circular cross section radius $\mathrm{r}_{mp}^{i}$. They are identified as effective fluids with the parameters ($\mathrm{k}_{mp}^{i}, Z_{mp}^{i}$) given by the JCAL model detailed in [1]. Thus, the thermal and the viscous characteristic lengths are equal to the radius $\mathrm{r}_{mp}^{i}$, the static flow resistivity is defined as $8\eta/\left(\mathrm{r}_{mp}^{i}\right)^{2}\phi$ with $\eta$ the dynamic viscosity of air, $\phi$ the open porosity equal to 1, and with the tortuosity equal to 1. The expression of a transfer matrix of a cylindrical pore $\mathrm{T}_{X}(\mathrm{h}_{X}, \mathrm{k}_{X}, \mathrm{Z}_{X})$ is given in the Appendix A, so that $\mathrm{T}_{mp}^{i} = \mathrm{T}_{X}\left(\mathrm{h}_{mp}, \mathrm{k}_{mp}^{i}, Z_{mp}^{i}\right)$.

As shown in see **Fig. 2**, the "full cavities" (dotted black outline area) are composed of an annular cavity (green area) and a common volume corresponding to the continuation of the main pores at the center of the cavity (white area). The thin annular cavities are modeled as lumped elements, detailed in the following. To account for the difference in main pore radius between cavities $i$ and $i + 1$, it is suggested to partition each full cavity matrix $\mathrm{T}_{F\_cav}^{i}$ into two cylindrical common pore

matrices $T_{com}^{i}$ and $T_{com}^{i+1}$, an annular cavity matrix $T_{A\_cav}^{i}$ defined through a lumped element and two matrices of sudden area discontinuities $T_{sect,1}^{i}$ and $T_{sect,2}^{i+1}$:

$$T_{F\_cav}^{i} = T_{com}^{i} T_{sect,1}^{i} T_{A\_cav}^{i} T_{sect,2}^{i} T_{com}^{i+1} \quad (3)$$

with $T_{A\_cav}^{i}$ a point matrix representing the annular cavity, and $T_{sect,1}^{i}$ and $T_{sect,2}^{i+1}$ account for the continuity of pressures and velocities between the junction of the two common pores and the annular cavity. All these three matrices correspond to element with zero thickness. A verification study of the analytical model with finite element results has shown that this intuitive segmentation, with the $T_{A\_cav}^{i}$ matrix positioned at the center of the element and section changes around it, is more suitable for this metamaterial with thin cavities. This contrast with other possible segmentations, such as the one used by Guasch et al. [19] with the $T_{A\_cav}^{i}$ matrix and section change positioned at the end of the element.

The presence of two common pores ($T_{com}^{i}$ and $T_{com}^{i+1}$) arises from the transition between the preceding ($T_{mp}^{i}$) and following ($T_{mp}^{i+1}$) main pores within the full cavities. Because $r_{mp}^{i} < R_{cav}$, this transition induces added lengths of the main pores $h_{add}^{i}$ at the beginning ($T_{com}^{i}$) and end ($T_{com}^{i+1}$) of full the cavity, which correspond to the end-effect correction described in [1]. With the geometric parameters of this study, it is calculated that $h_{add}^{i} > h_{cell}/2$. It is therefore suggested to use matrices of common pores $T_{com}^{i}$ with a length of $h_{cav}/2$ that are joined in the middle of the full cavity with the following one. $T_{com}^{i}$ has the same effective fluid parameters as $T_{mp}^{i}$, so $T_{com}^{i} = T_X\left(h_{cav}/2, k_{mp}^{i}, Z_{mp}^{i}\right)$.

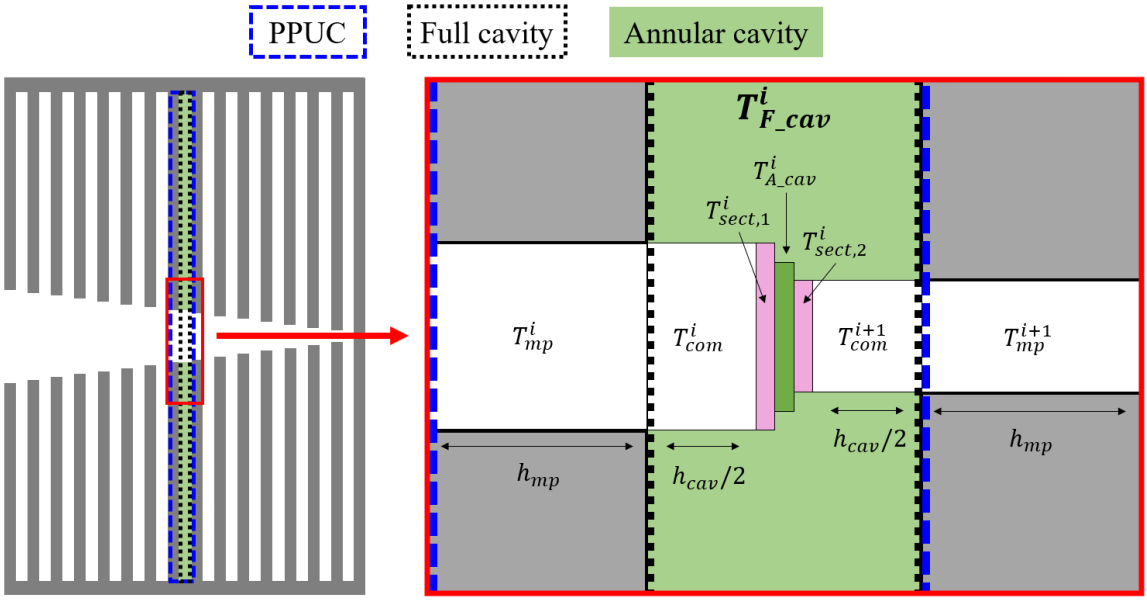


**Fig. 2.** Detail of one full cavity surrounded by two main pores of the metamaterial used in the analytical model

The annular cavities are considered as a lumped elements each with a surface impedance $Z^i_{S,cav}$, detailed in the following. Dupont et al. [12] suggest adapting the surface impedance expression of a thin annular cavity from [24] and identifying the cavities as equivalent fluids with wavenumber and characteristic impedance ($k_{cav}$, $Z_{cav}$), given by JCAL model [1]. As the cavity thickness is much smaller than its radius, the wave propagation is considered radial, thus, the thin annular cavities are identified as slits so that the thermal and the viscous characteristic lengths are equal to $h_{cav}$, the static flow resistivity is defined as $12\eta/{h_{cav}}^2\phi$ with $\phi$ the open porosity equal to 1 and the tortuosity equal to 1. Then, the cavity, in green in **Fig. 2**, is not completely annular as the central perforation is composed of two successive cylinders with different radii, $r^i_{mp}$ and $r^{i+1}_{mp}$. This volume is however approximated by an annular cavity with outer radius $R_{cav}$ and inner radius $r^i_{in}$ defined by arithmetic mean $r^i_{in} = \left(r^i_{mp} + r^{i+1}_{mp}\right)/2$ to represent the resonant volume as accurately as possible. Therefore, the expression of the surface impedance of an annular cavity is as follows:

$$\mathrm{Z}^{i}_{S,\mathrm{A\_}cav} = jZ_{cav}\frac{H_0^{(1)}\left(k_{cav}r_{in}^{i}\right) - H_0^{(2)}\left(k_{cav}r_{in}^{i}\right)H_1^{(1)}(k_{cav}r_{cav})/H_1^{(2)}(k_{cav}r_{cav})}{H_1^{(1)}\left(k_{cav}r_{in}^{i}\right) - H_1^{(2)}\left(k_{cav}r_{in}^{i}\right)H_1^{(1)}(k_{cav}r_{cav})/H_1^{(2)}(k_{cav}r_{cav})} \quad (4)$$

with $H_a^{(b)}$ the Hankel function of a[th] order and b[th] kind. The transfer matrix which accounts for the annular cavity and its connections to the common pore at its center is given by:

$$\mathrm{T}^{i}_{A\_cav} = \begin{bmatrix} 1 & 0 \\ \dfrac{1}{\mathrm{Z}^{i}_{S,\mathrm{A\_}cav}}\dfrac{A^{i}_{cav}}{A^{i}_{int}} & 1 \end{bmatrix} \quad (5)$$

with $A^{i}_{cav} = 2\pi r^{i}_{int}h_{cav}$ the inner cylindrical area of the annular cavity also called "curtain area" in [24], and $A^{i}_{int} = \pi {r^{i}_{int}}^{2}$ its cross-section area.

Transfer matrices for sudden area discontinuities are also used to join the matrices $\mathrm{T}^{i}_{com}$, $\mathrm{T}^{i}_{A\_cav}$ and $\mathrm{T}^{i}_{com}$ which have three different radii. The $\mathrm{T}^{i}_{sect,1}$ matrix changes from section $A^{i}_{mp} = \pi {r^{i}_{mp}}^{2}$ to $A^{i}_{int}$, and the $\mathrm{T}^{i}_{sect,2}$ matrix from section $A^{i}_{int}$ to section $A^{i+1}_{mp} = \pi {r^{i+1}_{mp}}^{2}$. Their expressions are provided in the Appendix A.

The transfer matrix of the total sample with a radius $\mathrm{R}_{samp}$ in the open-open configuration is given by:

$$\mathrm{T}_{samp} = \mathrm{T}^{in}_{sect}\,\mathrm{T}_{in}\,\mathrm{T}_{mat}\,\mathrm{T}_{out}\,\mathrm{T}^{out}_{sect} \quad (6)$$

with $\mathrm{T}_{in}$ and $\mathrm{T}_{out}$ the input and output matrices corresponding to the cylindrical transfer matrices of the end-effect corrections defined in [1], and $\mathrm{T}^{in}_{sect}$ and $\mathrm{T}^{out}_{sect}$ corresponding to the transfer matrices for sudden area discontinuities at the input and the output of the sample.

The normal incidence reflection coefficient of the sample backed by a rigid wall as shown in **Fig. 1** and **Fig. 2**, is defined using the coefficients of the $\mathrm{T}_{samp}$ matrix:

$$\mathrm{R} = \frac{T_{samp,11} - T_{samp,21} Z_0}{T_{samp,11} + T_{samp,21} Z_0} \tag{7}$$

with $Z_0$ the characteristic impedance of the air.

The normal incidence absorption coefficient of this configuration is therefore:

$$\alpha_N = 1 - |\mathrm{R}|^2 \tag{8}$$

Finally, the impedance of a resonant full cavity is used in the following parts of this study and, assuming zero velocity at matrix output, it can be defined with the coefficient of the $\mathrm{T}^i_{F\_cav}$ matrix as:

$$\mathrm{Z}^i_{F\_cav} = \frac{T^i_{F\_cav,11}}{T^i_{F\_cav,21}} \tag{9}$$

### 2.3. Numerical Model

This section details the numerical model used to verify the proposed analytical model. A Finite Element Model (FEM) is implemented using the commercial software COMSOL Multiphysics® v. 5.6. The material is modeled within a cylindrical impedance tube to conduct virtual measurements and the absorption coefficient under normal incidence is obtained using the two-microphone method [25]. To minimize the computational time, a two-dimensional axisymmetric model is employed, taking advantage of the system's radial symmetry (see **Fig. 3** a) and b)). It is assumed here that the solid walls have infinite rigidity, thereby excluding any consideration of frame vibrations. The simulations are done with a Thermo-Visco-Acoustic (TVA) module which solves the full system of equations of fluid dynamics in the built geometry: the continuity equation, the momentum conservation equation, the energy conservation equation and the linearized equation of state, all recalled in [14]. The general mesh is made with triangular elements. Thin

quadrilateral elements are added to take into account all the boundary layer effects along the walls of the main pores and annular cavities (see **Fig. 3** c) and d)). A mesh convergence analysis has been done to minimize the computation time and ensure the simulations are mesh-independent.

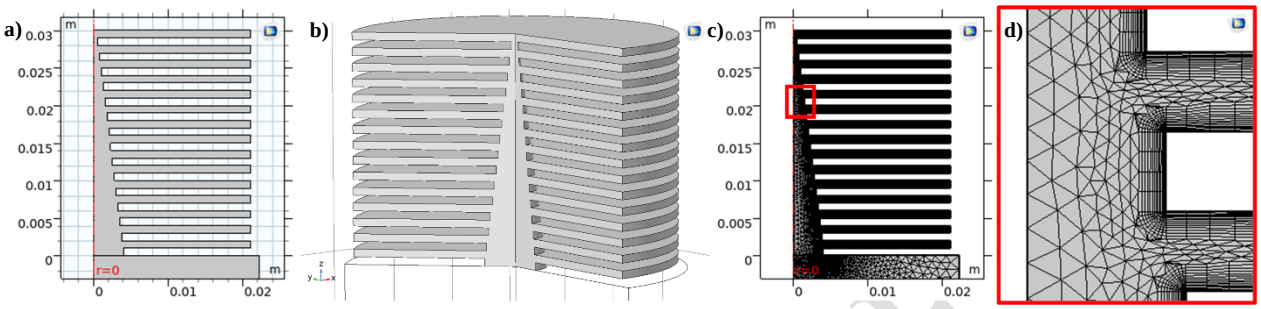


**Fig. 3.** Modeling of the material on COMSOL Multiphysics® v. 5.6: a) 2D axisymmetric and b) 3D equivalent representation of the modeled material; c) global view and d) zoom of the used mesh in an axisymmetric 2D view



### 2.4. Sample manufacturing and experimental setup

The proposed approach aims to validate the analytical and numerical models through laboratory measurements of sound absorption coefficient of the metamaterial. The sample is designed as an assembly of multiple plates perforated at their center (see **Fig. 4**) with cavities between them. The set of plates that have been fabricated allows for building metamaterials with different main pore radius profiles. In order to minimize air leakage, a preliminary study was conducted to optimize the contact point geometry between two successive plates. The metamaterial is made of aluminum alloy 6061 T6 (see **Fig. 4** c)) and manufactured using a machining method with a precision of $\pm$ 0.025 mm for the general geometry and drill main pore perforations as small as 0.5 mm. Compared to a 3D printing method, machining allows for flatter and smoother surfaces, and it better reproduces designed geometries such as cylindrical main pores, which is crucial as losses are concentrated in those regions.

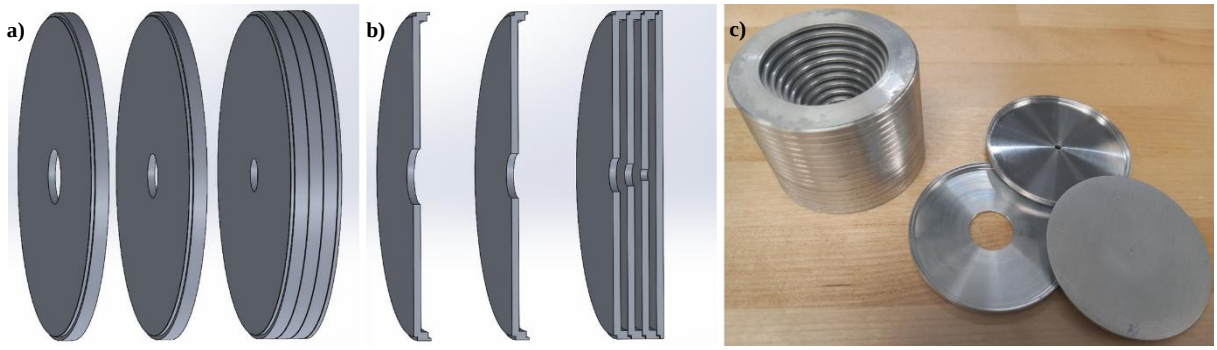


**Fig. 4.** Design of the manufactured technical solution: a) 3D global view and b) 3D cross-section of the modelling of single and assembled parts; c) picture of single and assembled parts machined in aluminum.

The normal incidence sound absorption coefficient is measured in an impedance tube with a radius $R_{tube} = 22.22$ mm and the two-microphone method is used [25]. In order to ensure the presence of plane waves within the tube, the measurements are performed in the frequency range of 100 Hz to 4 200 Hz. The sound pressure excitation is a white noise at 90 dB. Each sample is tested 5 times and each constituent cell is randomly selected from the batch with the desired radius for the purpose of repeatability. The results are presented with the mean value "EXP average" and the range of values "EXP scatterplot".



## 3. Results

### 3.1. Validation of the analytical model

The TMM and FEM simulations as well as the measurements of the normal incidence sound absorption coefficient of the metamaterial with constant profile $r_{mp}^{i} = 2$ mm $\forall i \in [1:15]$ are presented in **Fig. 5** a). This material corresponds to sample *B* proposed by Dupont et al. [12]. The first five absorption peaks have almost identical values and frequencies for the FEM predictions and the experimental results, with the TMM predictions being very close as well. The band gap corresponds to the frequency zone where waves do not propagate. Here, the beginning of the band

gap, occurring around 2 500 Hz, is also similar for the TMM and FEM simulation with a slightly lower frequency observed in the experimental data. The good agreement between the TMM and FEM predictions as shown in **Fig. 5** a) suggests that accounting for losses in the "common pore" in the TMM via an equivalent fluid model is relevant. The measurement variability is very small (grey surface) in the whole frequency range of interest suggesting that the PPUC used in the assembly are very similar and that air leakage between the plates is minimal. Interestingly, the acoustic behavior of the sample fabricated in this work is in better agreement with the simulations compared with sample *B* in [12] (see Fig. 7 of this reference) which has the same geometry but was fabricated in ABS with a 3D printing process. This can be attributed to a better control over the geometry, such as more circular main pores, flatter cavity walls, and smoother surfaces. Additionally, air leakage is minimized with well-fitted elements, and vibration effects are reduced within the studied frequency range by using a more rigid plate material.

**Fig. 5** b) shows the sound absorption curves of the metamaterial having a linearly ($p = 1$) decreasing main pore profile from $r_{mp}^{1} = 4$ mm to $r_{mp}^{15} = 0.5$ mm. The first absorption peak is almost identical for the three curves, but discrepancies can be observed for the following peaks, mainly for the TMM simulations (blue curve in **Fig. 5** b)). These differences may be attributed to the simplified modeling of the end-effect, which assumes common pores of constant thickness and may not fully capture the complexity of the acoustic field in the cavities. However, the average level of the absorption coefficient below 2 700 Hz is very similar among the three curves. It is worth noting that there are fifteen distinguishable absorption peaks in both TMM and FEM simulations, corresponding to the number of resonances in a fifteen-degree-of-freedom system. The beginning of the band gap is similar for the TMM and FEM simulations around 3 250 Hz and occurs at lower frequencies (around 2 900 Hz) in the measurement. The measurement variability

is more important above 2 500 Hz, although still satisfactory. Additionally, the measured absorption coefficient is shown to increase around 4 000 Hz which could be attributed to the vibration of the structure. An additional numerical analysis has been carried out to study the influence of plates vibration. The frequency of the first vibrational mode of the annular plates ranges from 5 348 Hz to 5 425 Hz, with a central perforation varying from 0.5 mm to 4 mm. For a plate with no central perforation (the last plate), it is 5 387 Hz. These frequencies were determined using finite element analysis assuming each PPUC is simply supported at this edge. Taking into account that in reality the boundary conditions are more complex, notably with the use of Vaseline to reduce air leakage, the vibration effects could account for the absorption increase around 4 000 Hz.

Furthermore, it is noteworthy that there seems to be a slight shift of the band gap towards lower frequencies in experimental results. This can, in part, be also explained by a structural vibration effect, as previously observed by Umnova et al. [21] (see Fig. 10 of this reference). In Appendix B, **Fig. 12** a) and b) present absorption curves of these two profiles either determined numerically (with rigid or elastic walls) and experimentally. It can be observed that considering wall vibration result in a slight shift in absorption towards lower frequencies, which partly accounts for the discrepancy between the models and experimental measurements. Additionally, this might also be attributed to discrepancies between the manufactured samples and the theoretical geometries, with potential machining imperfections and slight defects along the edges of the central perforation due to burr removal.

Despite these differences, the absorption curve, including amplitude, frequency, and the number of peaks, remains consistent and satisfactory across the results. This section validates the TMM model, confirms the suitability of the rigid TVA FEM, and demonstrates the manufactured sample

quality. The TMM model will now be used to investigate how variations in the main pore profile impact the acoustic characteristics of the metamaterial.

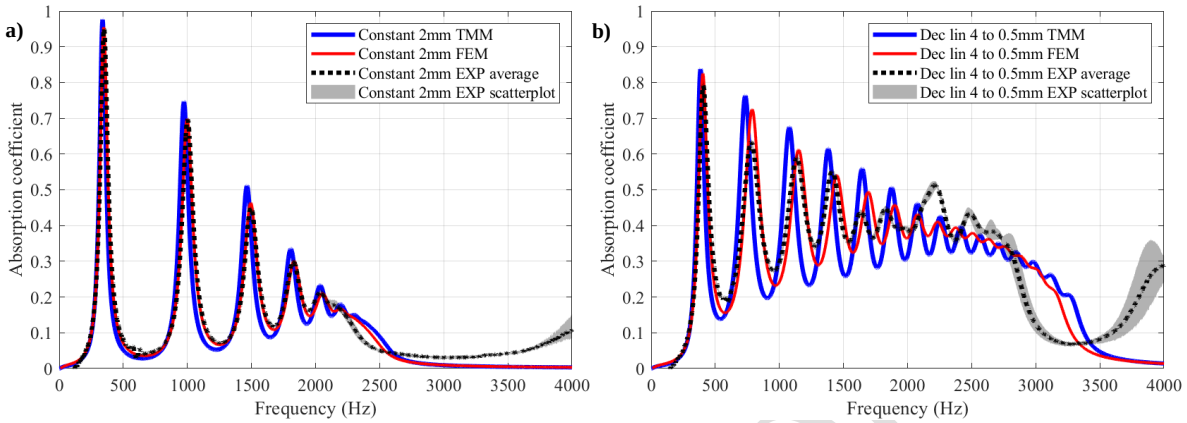


**Fig. 5.** Comparison of the absorption coefficient for a) a metamaterial with constant profile $r_{mp} = 2$ mm and b) a metamaterial with profile decreasing linearly from 4 mm to 0.5 mm according to the TMM, the FEM and experimental results.

### 3.2. Constant main pore profiles analysis

In this section, the primary focus is on the metamaterial with a constant main pore radius to develop a comprehensive understanding of its effect on the sound absorption peaks. For this purpose, the TMM model, along with the complex frequency plane representation, is employed.

The absorption coefficient of four metamaterials with constant profile are depicted in **Fig. 6** a) namely $r_{mp} = 1$ mm (green curve), $r_{mp} = 2$ mm (black curve), $r_{mp} = 3$ mm (blue curve) and $r_{mp} = 4$ mm (red curve). The local resonance frequencies of a full cavity for these metamaterials are also denoted by vertical dashed lines (with corresponding colors). These resonance frequencies are calculated from the acoustic impedance of a full cavity (Eq. (9)) and correspond to the frequency at which the imaginary part equals to zero. **Fig. 6** a) shows that these resonance frequencies initiate the band gap. However, in the case of metamaterials with non-constant profiles, Umnova et al. [21] demonstrated that it is the resonance frequency of the first cavity that

initiates the band gap. Increasing $r_{mp}$, as shown in **Fig. 6** a) always leads to the increases of the first peak frequency. As to the amplitude of the first peak, it first increases from 0.48 (in green) to 0.98 (in black) and then decreases to 0.94 (in blue) and 0.79 (in red). This first peak depends on the global geometric parameter of the metamaterial [12] [13] and the perfect absorption (peak value $= 1$) is reached for $r_{mp} = 2.25$ mm (not shown here).

The complex frequency plane representation of the reflection coefficient of the metamaterial with $r_{mp} = 2$ mm is plotted in the background of **Fig. 6** b). The resonances of a system are represented by a pair of poles (local maxima) and zeros (local minima) at the same real frequency [21]. In more detail, this is shown for the metamaterial with $r_{mp} = 2$ mm in Appendix C, **Fig. 13**. Perfect absorption corresponds to a zero positioned on the real frequency axis (imaginary part of frequency = 0). If the zero is positioned below this axis, the losses are too strong to achieve perfect absorption, and conversely, if the zero is above it, the losses are too weak. For this configuration ($r_{mp} = 2$ mm), solid black markers indicate the first six zeros and are connected together by a dashed line with the corresponding color. The first six zeros of the three other constant profile configurations represented in **Fig. 6** a) are also presented in **Fig. 6** b) and are connected by a dotted line (with corresponding colors). These lines can quantify the equilibrium of losses among the modes. The more horizontal the line, the more balanced the losses of all modes will be and hence the perfect absorption could be reached for all of them. For example, to achieve perfect absorption peaks for the $r_{mp} = 3$ mm profile (blue markers and dotted line), it is necessary to adjust losses at each mode in different way. The first mode's zero lies slightly above the real frequency axis, so a slight increase in losses is required to attain a perfect absorption peak. Conversely, the second zero, situated slightly below the real frequency axis, would necessitate a slight reduction in losses.

Subsequent zeros would require progressively larger reductions in losses. However, it is observed that the dotted lines maintain oblique orientation with a similar angle from $r_{mp} = 0.5$ mm to $r_{mp} = 5$ mm for a constant profile, suggesting persistent imbalance in the losses.

An additional observation can be made regarding the size of the color spots shown in **Fig. 6** b). The absorption curve corresponds to the real frequency axis of the complex frequency plane. Therefore, the size of the color spot is directly related to the width of the corresponding absorption peak. In Appendix C **Fig. 14**, the complex frequency plane representations are shown for the four constant profiles considered in this section. They show the first zero of each profile, maintaining the same scale, and regions of equal absorption have been added for convenience. It can be observed that as the radius $r_{mp}$ increases, the size of the color spot around zero also increases (**Fig. 14**), resulting in a broader absorption peak (shown in **Fig. 6** a)).

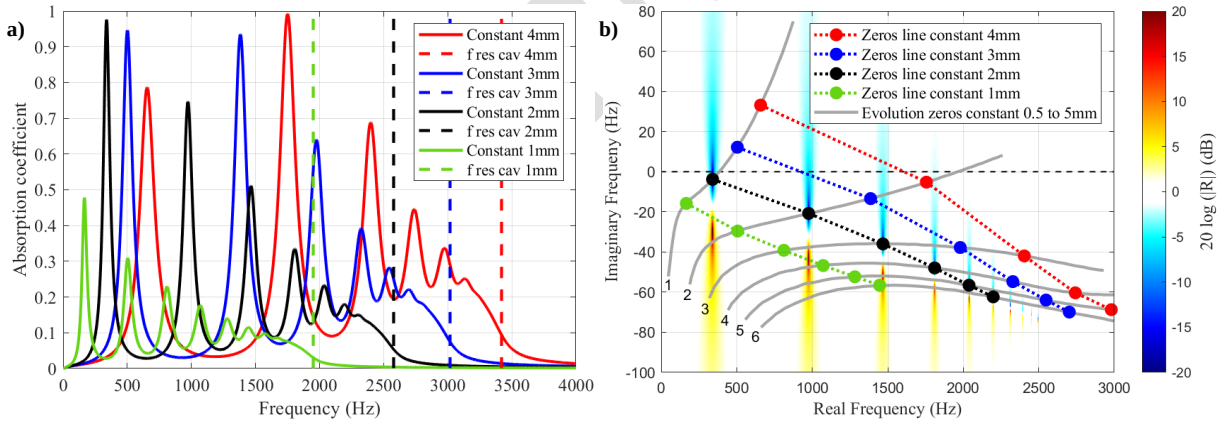


**Fig. 6.** a) Absorption coefficient for metamaterials with constant main pore radius and the resonance frequencies of corresponding cavities; b) Complex frequency plane representation of 20log(R) for metamaterial with $r_{mp} = 2$ mm and the evolution of the first 6 zeros positions for metamaterials with $r_{mp}$ ranging from 0.5 to 5.5 mm; positions corresponding to the four metamaterials from a) are marked and connected.

Further analysis using different combinations of geometric parameters, including variations in $h_{mp}$ and $h_{cav}$ values, while maintaining a constant profile and a periodic metamaterial structure, leads to the same conclusion. Hence, it can be inferred that a constant main pore profile does not allow the perfect absorption at multiple peaks. Therefore, the following sections aim to explore

metamaterials with varying profiles of the main pore to effectively enhance absorption across multiple peaks by balancing losses.

### 3.3. Continuous variations of the main pore

In this section, multiple continuous profiles of $r_{mp}$ are studied in order to determine the arrangement for a better absorption over a broad frequency range. Then, the influence of local resonances will be examined to improve the understanding of their influence on the acoustic properties.

First, three metamaterials with decreasing, constant, and increasing main pore profiles are compared (see **Fig. 7** a) and b)). The profiles are linear ($p = 1$) and share a common value for the radius of the first main pore $r_{mp}^{1} = 3$ mm. This ensures that their band gaps start at the same frequency, as described in [21]. The decreasing profile exhibits a greater number of absorption peaks at lower frequencies (**Fig. 7** b)). This can be attributed to the enhanced effects of the larger annular cavities as the radius of the main pore decreases, as seen in **Fig. 6** a). This can be attributed to an amplified "dead-end" effect, leading to a lower effective bulk modulus of the air within the material [11] [12]. On the other hand, the increasing main pore profile shows only five spaced peaks in its absorption curve.

The resonance frequency of each full cavity as defined using Eq. (9) are shown in **Fig. 7** c) and d) (dashed-dotted vertical line). The size of the main pores corresponding to the full cavity directly influences its resonance frequency. In the case of metamaterial with increasing main pore profile (see **Fig. 7** c)), all local resonance frequencies are higher than that of the first full cavity and do not lead to absorption peaks. The few observable absorption peaks are referred to as the "global resonances" of the material in [21] and correspond to resonances along the structure. Conversely,

in the case of metamaterial with decreasing main pore radius (see **Fig. 7** d)), the lowest resonance frequency is associated with the 15$^{th}$ full cavity, it further increases until reaching the resonance of the first full cavity. All local resonances of the full cavities contribute to the overall absorption of the metamaterial before the band gap. Notably, the absorption peaks in the range of 2 000 Hz and 3 000 Hz are very close together creating a continuous absorption band. Therefore, decreasing profiles enhance the acoustic performance of the metamaterial by introducing noticeable local resonances giving a more pronounced clustering effect and increased visibility of absorption peaks. In the following, the effect of the metamaterial geometrical parameters on its acoustic response is investigated. This involves examining the effects of cavities based on their specific positions within the structure. For an ABH profile, Umnova et al. [21] has shown that beyond a resonant cavity, the equivalent sound speed remains very close to zero, and as a result, wave propagation is strongly limited beyond that cavity. Thus, above this frequency, only the cavities preceding the resonating one will contribute to the absorption. This phenomenon can be illustrated using truncated metamaterials (see **Fig. 7** e and f)). Above the resonance frequency of a cavity within an ABH profile, the absorption coefficient of the truncated metamaterial, becomes equivalent to that of the entire structure. Thus, the subsequent cavities have no influence on the absorption, confirming that the cavity behaves as a rigid wall after its resonance frequency.

Consequently, the last cavity (here the 15$^{th}$ cavity) influences the absorption up to its resonance frequency and therefore affects the first few peaks. Conversely, the first cavity will influence the entire absorption range the gap band. This implies that the low frequency absorption peaks are influenced by all the cavities in the metamaterial, while the peaks at higher frequencies are only controlled by the first cavities of the metamaterial. This understanding is used in the following sections to analyze different ABH metamaterial profiles.

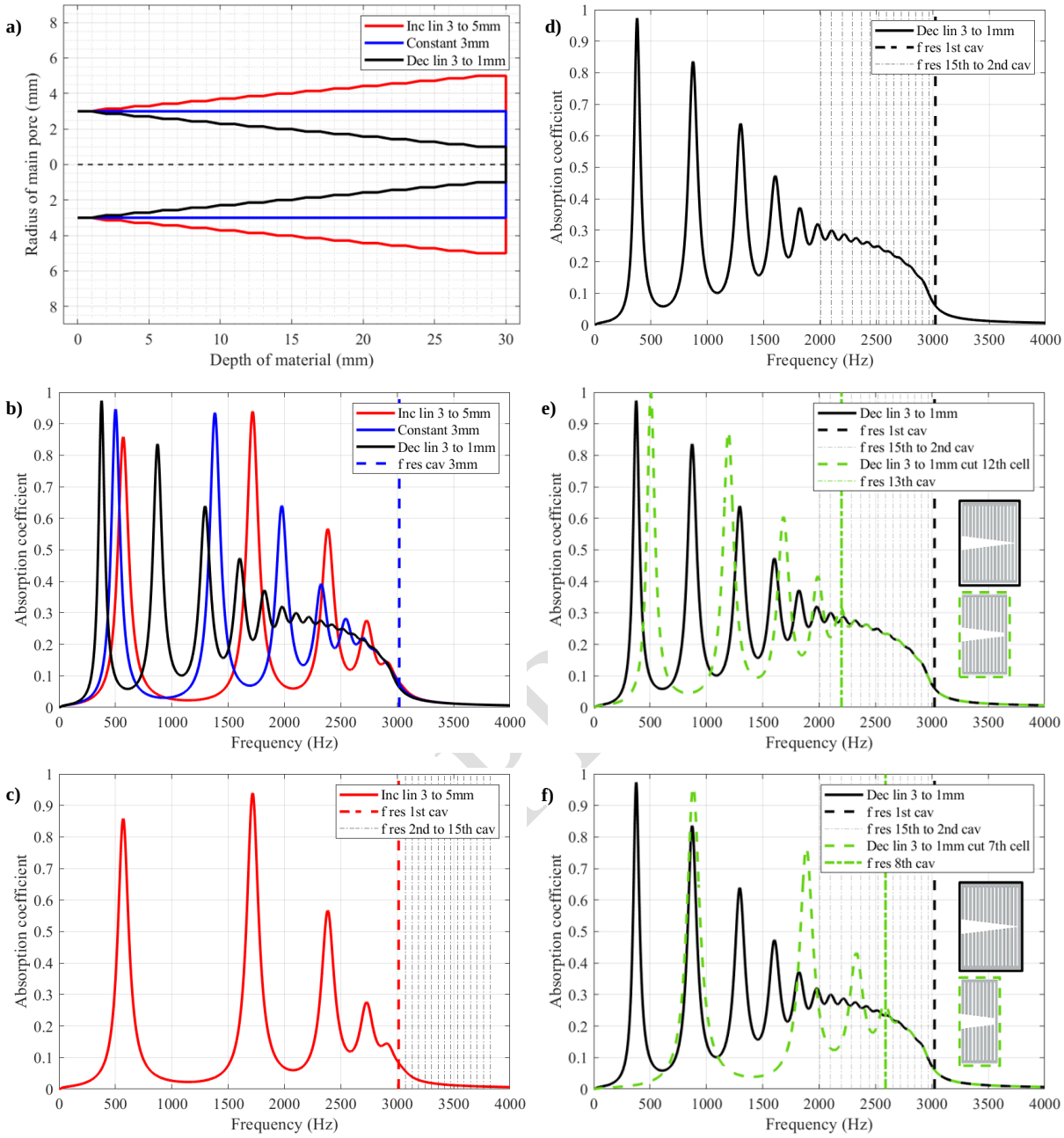


**Fig. 7.** a) Dependence of the main pore radius on the depth for three metamaterials with continuous profile, b) their absorption coefficient and the resonance frequency of a cavity with $r_{mp} = 3$ mm; Absorption coefficient and the 15 resonance frequencies of all their cavities of metamaterial with c) an increasing and d) a decreasing profile; Absorption coefficient for the metamaterial with decreasing profile and the same material truncated after e) the 12$^{th}$ or f) the 7$^{th}$ cell.

### 3.4. Parametric study of ABH profiles

In the previous section, it was shown that ABH profiles offer greater potential for enhancing the acoustic performance of the metamaterial, due to the presence of absorption peaks caused by local resonances preceding the band gap. This section presents a parametric study of ABH profiles to further investigate their impact on the acoustic behavior of the metamaterial. First, the analysis focuses on linear decreasing profiles, where the radius of the first main pore is varied, followed by the radius of the last main pore. Subsequently, a parameter characterizing non-linearity of ABH profiles is introduced. The investigation of these three parameters aims at understanding how to achieve a balance of losses among the resonances, for a broadband performance.

#### 3.4.1. Linear profiles

A comparative analysis of several metamaterials with linearly decreasing $r_{mp}$, while keeping one parameter ($p$) constant, provides insights into the impact of the main pore radii. A linear ABH profile can be fully characterized by the radii values of the first main pore ($r_{mp}^{1}$) and the last main pore ($r_{mp}^{15}$), corresponding respectively to the maximum and the minimum radii.

First, the influence of the value of $r_{mp}^{1}$ is analyzed. Three metamaterials with a linearly decreasing main pore profile are studied with the last cavity fixed at $r_{mp}^{15} = 1$ mm and the first cavity having $r_{mp}^{1} = 4$ mm, $r_{mp}^{1} = 3$ mm and $r_{mp}^{1} = 2$ mm (see **Fig. 8** a), b) and c)). As expected, the band gap shifts to higher frequencies as the radius of the main pore in the first cavity increases. It influences the resonance frequency of a full cavity, resulting in increased absorption peaks and reduced losses across all modes. The modes exhibit $20\log(R)$ zeros below the real frequency axis on the complex plane (see **Fig. 8** c)). To raise them and enhance absorption, loss reduction is necessary.

However, balancing losses and aligning all zeros on the same horizontal line is not possible due to the simultaneous impact of the first cavity on all modes. Nonetheless, adjusting the size of the main pore in the first PPUC allows for control of overall loss and the starting frequency of the band gap.

Next, the influence of the smallest pore radius $r_{mp}^{15}$ in the last PPUC of the metamaterial is analyzed. Three metamaterials with linearly decreasing profiles are compared, with a fixed main pore radius of the first cavity $r_{mp}^{1} = 4$ mm, but different smallest pore radii (see **Fig. 8** d) e) and f)). As expected, the three metamaterials have the same band gap starting frequency due to the constant $r_{mp}^{1}$ value. Absorption peaks shift towards lower frequencies as the radius of the last main pore decreases, due to the influence of a larger annular cavity on the reduction of the effective bulk modulus. For example, the metamaterial with the decreasing profile from $r_{mp}^{1} = 4$ mm to $r_{mp}^{15} = 0.5$ mm exhibits 6 absorption peaks below 2 000 Hz (see blue curve in **Fig. 8** e)), whereas the metamaterial with the decreasing profile from $r_{mp}^{1} = 4$ mm to $r_{mp}^{15} = 3$ mm has only 2 peaks (see orange curve in **Fig. 8** e)). This behavior is further confirmed by the complex frequency plane representation of the reflection coefficient (see **Fig. 8** f)), where the imaginary frequency of the first zeros decreases as the radius of the last main pore decreases. Additionally, the imaginary frequency of the last zeros is minimally affected by $r_{mp}^{15}$, as the last cavities of a metamaterial with a decreasing profile only influence the low frequency modes. Notably, the lines connecting the zeros progressively approach a horizontal position compared to a constant profile, indicating a gradual balancing of losses in the metamaterial.

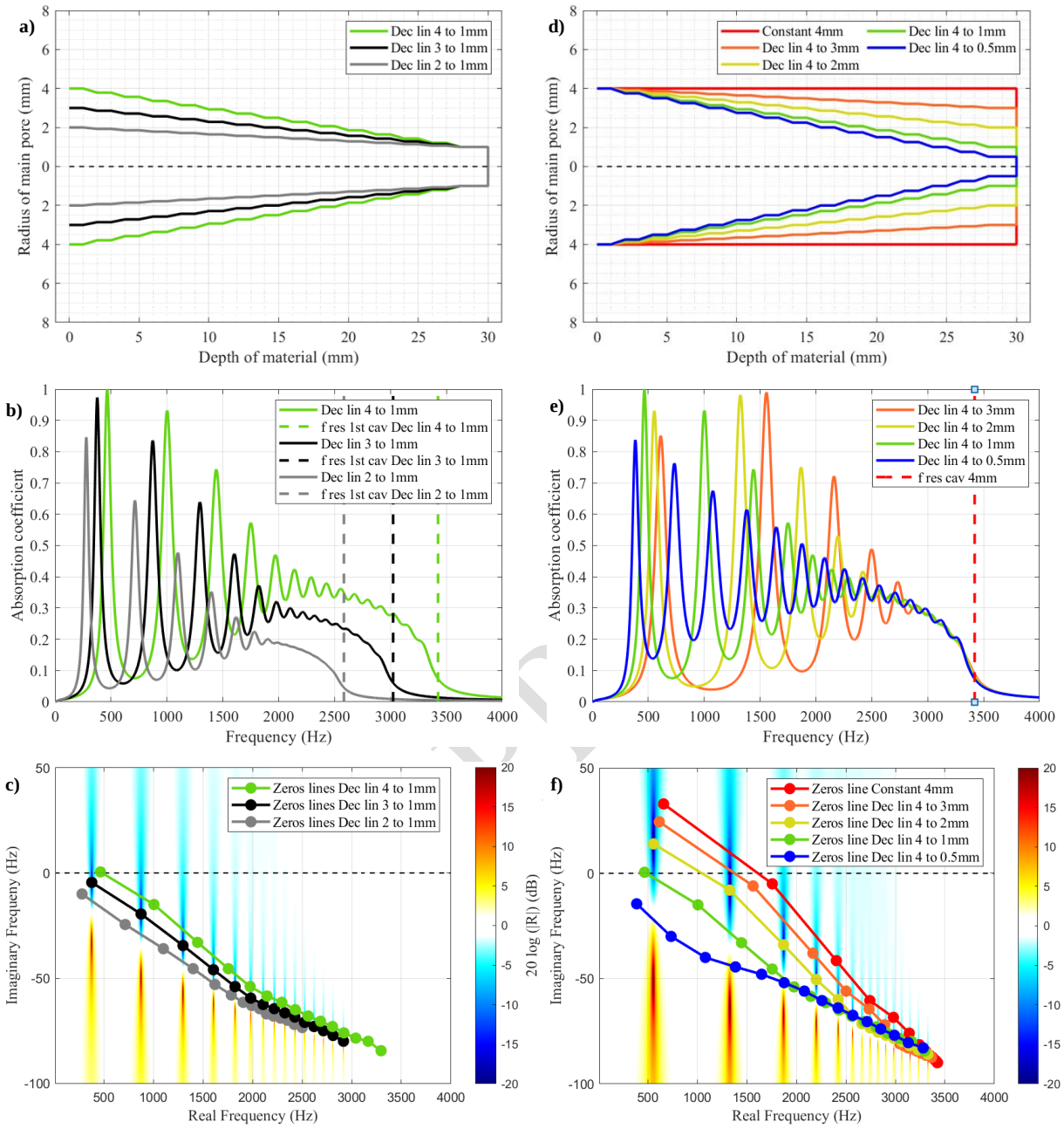


**Fig. 8.** a) Dependence of the main pore radius on the depth for three metamaterials with decreasing profile with various first radii, b) their absorption coefficient and the resonance frequency of their first cavity and c) the complex frequency plane representation of 20 log(R) (corresponds to black line in b)) with the positions of the 15 zeros for the three metamaterials marked and connected;
d) Dependence of the main pore radius on the depth for five metamaterials with decreasing profile with various last radii, e) absorption coefficient for four of them and the resonance frequency of the $r_{mp} = 4$ mm cavity and f) the complex frequency plane representation of 20 log(R) (corresponds to yellow line in e)) with the positions of the 15 zeros for the five metamaterials marked and connected.

Therefore, the parameter $r_{mp}^{1}$ controls the lower band gap boundary, the frequency position of absorption peaks, and the level of losses across all modes. Conversely, reducing $r_{mp}^{15}$ helps in balancing losses by increasing them for the first modes and simultaneously making resonance frequencies lower. However, for the profiles considered in this study, this approach proved insufficient to achieve complete loss balancing. Additionally, it should be noted that $r_{mp}^{15}$ cannot be reduced below 0.5 mm due to manufacturing process limitations.

### 3.4.2. Non-linear profiles

In this section, non-linearly decreasing profiles of the main pore radius are studied to accentuate loss balancing among the modes and reach perfect absorption for a maximum number of absorption peaks. For this purpose, the parameters $r_{mp}^{1}$ and $r_{mp}^{15}$ are kept constant, with only the parameter $p$ in eq. (1) being varied. Shown in **Fig. 9** a), the $p = 2$ profile (see red curve), is characterized by a slow decrease at the beginning and a rapid decrease towards the end of the metamaterial. The $p = 1$ profile (see blue curve) is a linear profile investigated in the previous section. The $p = 0.5$ profile (see green curve) exhibits a rapid decrease at the entrance of the metamaterial and a slower decrease towards the end. In **Fig. 9** b), the amplitude of absorption peaks at low frequencies increases with $p$, while the peaks at medium frequencies remain unchanged (see red curve). Conversely, decreasing $p$ (see green curve) mainly impacts the peaks at low frequency. These observations are a result of the simultaneous alteration of losses in all cavities due to the modification of $p$ in the profile. The low frequency absorption undergoes significant modification as it depends on all cavities. In contrast, the absorption peaks at higher frequencies, which rely on only a few front cavities, are less affected. This is further confirmed by

the complex frequency plane representation of the reflection coefficient (see **Fig. 9** c)), where the lines connecting the zeros become more horizontal for a smaller $p$. As a result, parameter $p$ balances losses between modes by primarily modifying the amplitude of low-frequency peaks. Thus, the $p = 2$ non-linear main pore profile exhibits highly varying amplitude absorption peaks, whereas the $p = 0.5$ profile shows absorption peaks with nearly the same amplitude across the frequency range considered. Therefore, an ABH main pore profile with $p < 1$ accentuates the losses of the low frequency peaks and modifies the higher frequency ones only slightly. This type of profile is well-suited for achieving a broadband metamaterial performance with multiple absorption peaks of similar amplitudes.

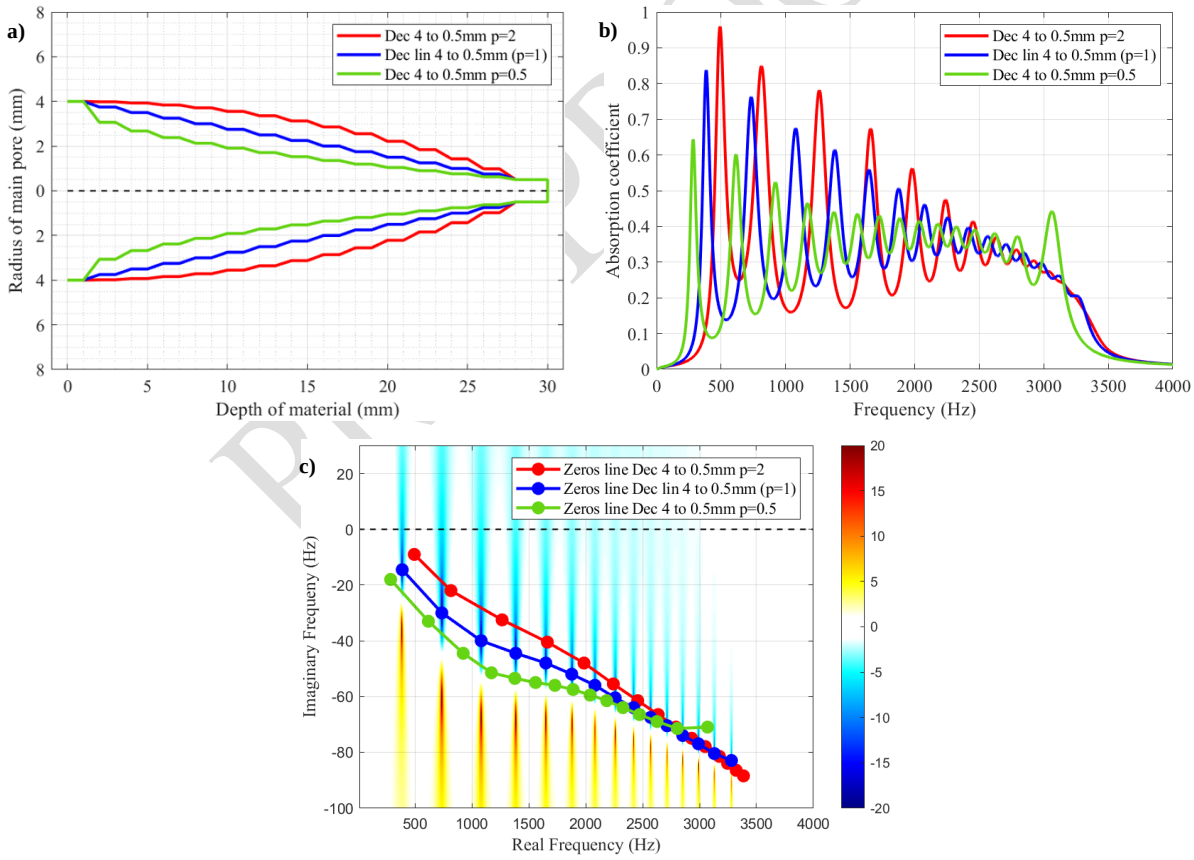


**Fig. 9**. a) Dependence of the main pore radius depending on the depth for three ABH profile with various $p$ coefficient, b) their absorption coefficient and c) the complex frequency plane representation of 20 log(R) (corresponding to the linear ($p = 1$) metamaterial with blue line) with the positions of the 15 zeros for the three metamaterials marked and connected.

### 3.5. Broadband ABH profiles

In this section, ABH metamaterial profiles with broadband absorption are designed based on the insights gained from the previous sections regarding the influence of parameters $r_{mp}^{1}$, $r_{mp}^{15}$ and $p$. Next, their absorption coefficients predicted by TMM are compared and validated through FEM simulations and experiments.

#### 3.5.1. Profile determination

Initially, the radius of the main pore at the metamaterial's entrance is determined to achieve a high amplitude of the higher frequency absorption peaks (see section 3.4.1, **Fig. 8** a)-c)) as it is the only parameter influencing them. A larger value of $r_{mp}^{1}$ is required to minimize losses in the higher frequency modes and bring the corresponding zeros closer to the real axis in the complex frequency plane representation of the reflection coefficient. Additionally, this results in shifting the onset of the band gap beyond 4 000 Hz. Subsequently, the main pore radius of the last cavity is reduced to shift the absorption peaks towards lower frequencies, as well as to introduce losses to the low frequency peaks in order to balance their amplitudes with those of the last peaks (see section 3.4.1, **Fig. 8** d)-f)). If further adjustments are necessary to ensure that the peaks have similar amplitudes, the parameter $p$ can be decreased to accentuate the effect of balancing the losses between the first and last modes (see section 3.4.2, **Fig. 9**). However, it is important to carefully consider the trade-offs between the amplitude of the absorption band and the position of the absorption peaks at low frequencies. Indeed, increasing $r_{mp}^{1}$ raises the last absorption peak amplitudes, simultaneously resulting in a shift of the resonances towards higher frequencies (see **Fig. 8** b) and c)). All these conclusions and interpretations are drawn from numerical tests conducted in the preceding sections.

Taking these conclusions into account, an investigation was carried out on the impact of varying these three key parameters on absorption values and frequencies, with the aim of obtaining practical insights into optimal parameter values. This allowed design of two metamaterial profiles, as shown in **Fig. 10** a) and b). The metamaterial with a profile corresponding to the green line is an ABH profile with $r_{mp}^{1} = 15$ mm, $r_{mp}^{15} = 1$ mm and $p = 0.8$. The one corresponding to a red line is an ABH profile with $r_{mp}^{1} = 11$ mm, $r_{mp}^{15} = 0.75$ mm and $p = 0.5$ The green absorption curve exhibits 7 absorption peaks below 4 000 Hz, very close to perfect absorption (>0.99) except for the second peak at 0.96. The first peak occurs at 1 002 Hz, and the second at 1 611 Hz. The metamaterial has band with an average absorption exceeding 0.82 between 2 050 Hz and 4 000 Hz, with absorption coefficient higher than 0.64 above 2 500 Hz. Then, the red absorption curve displays 12 absorption peaks below 4 000 Hz, with peaks at lower frequencies ($f_1 = 603$ Hz and $f_2 = 1\,136$ Hz). This material also has an absorption band at lower frequencies, albeit with a slightly lower amplitude, with an average absorption above 0.69 between 1 500 Hz and 4 000 Hz. These two profiles provide insights into the trade-offs between the amplitude of the absorption band and the low frequency position of the absorption peaks. For the comparison purpose, the absorption curve of an aluminum foam sample with the same thickness (30 mm) as these metamaterials is also represented in blue dashed line. The calculations are performed using a JCA model with parameters derived from Dupont et al. [26]. This foam was selected because it is dedicated to the same type of harsh environments, such as engines or reactors. The absorption curve of the foam material exhibits a broad peak at medium frequencies but also a significant decrease at higher frequencies. Therefore, the metamaterials studied here perform better at lower frequencies for tonal absorption and can also provide good broader-band absorption at higher frequencies.

**Fig. 10** c) and d) show the complex frequency plane representation of reflection coefficient of the two metamaterials, with solid round markers indicating the position of the zeros in green (c) or red (d). For the ABH profile corresponding to green lines, the zeros are really close to the perfect absorption line and remain well aligned overall, corroborating the findings in **Fig. 10** b). As previously mentioned, a zero on (or close to) the real frequency axis enables perfect (or enhanced) acoustic absorption, corresponding to an absorption peak with an amplitude of 1 (or close to 1) [22]. Regarding the ABH profile corresponding to red lines, although not all the zeros are exactly on the real frequency axis, they are nearly aligned, indicating a general well-balanced distribution of losses between the modes. The regions of equal absorption around the zeros intersect the real frequency axis, which is consistent with the absorption curves. Furthermore, there is a significant difference in the size of the color spots around the zeros between these two profiles. This highlights the limitations of a study that only considers the position of the zeros, as the size of the color spot around them also have a direct relationship with the width of the absorption peaks. However, this can be explained by extending the conclusions about the size of the color spot around zero made for the constant profile materials (see section 3.2 and Appendix C, **Fig. 14**). It has been observed that as the radius of the constant profile increases, the size of the color spot around zero also increases, resulting in a wider absorption peak. Here, the profile corresponding to green color has larger pore radii than the profile corresponding to red, which appears to account for the larger size of zones around zeros and broader absorption peaks. An extensive examination of this effect would be of interest but pose significant complexity due to strong coupling between the resonances.

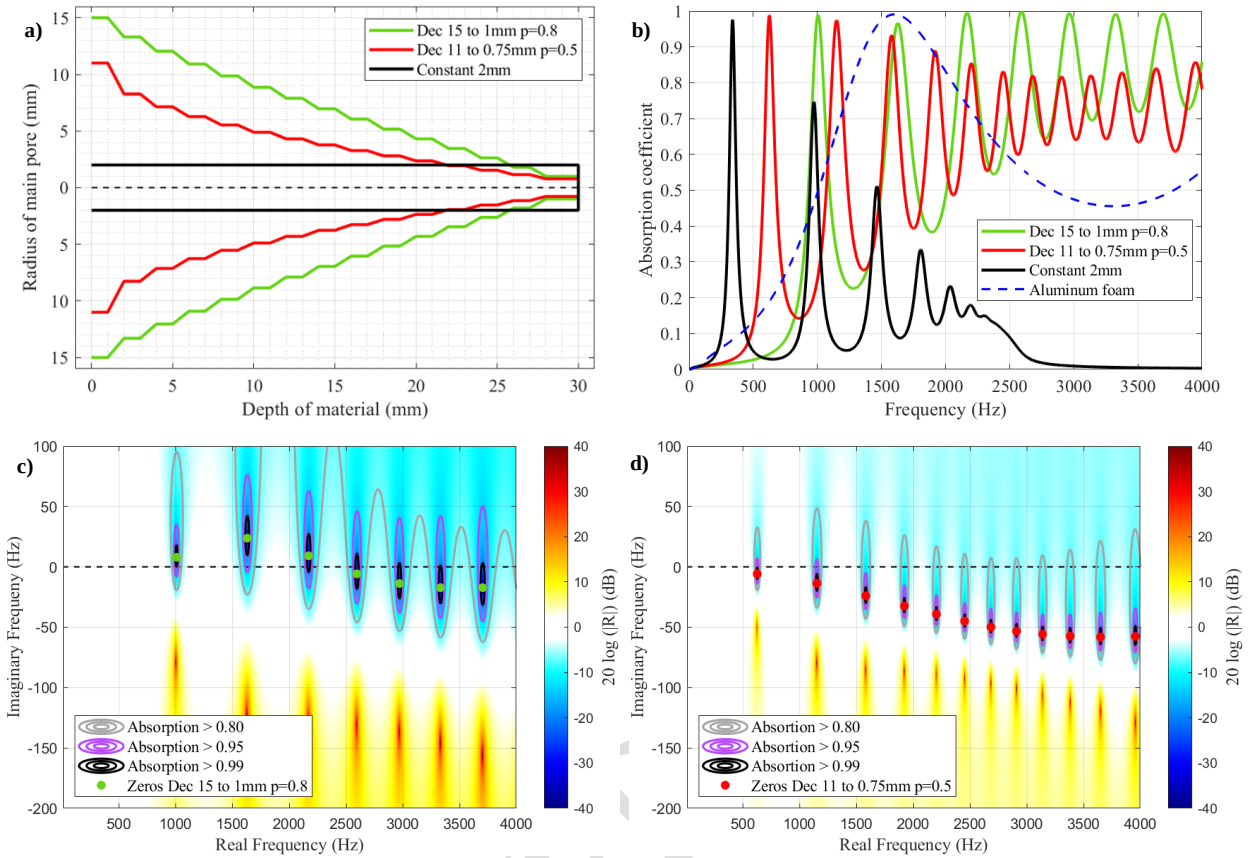


**Fig. 10.** a) Dependence of the main pore radius on the depth for two ABH broadband metamaterials and the metamaterial with constant profile $r_{mp} = 2$ mm, b) their absorption coefficient and that of aluminum foam, and c)-d) the complex frequency plane representation of 20 log(R) for the two ABH broadband metamaterials with the positions of their 15 zeros marked and the iso-absorption zones indicated;

### 3.5.2. Validation of the results for broadband profiles

To validate the TMM results for the two profiles with broadband performance by comparing with the FEM and experiments, the metamaterials were fabricated as described in Section 2.4.

In **Fig. 11** a), a good correlation between TMM and FEM results concerning the amplitude of the absorption peaks can be observed. The first three absorptions peaks have the same frequencies, but beyond that, there is a gradual shift toward lower frequencies as the frequency increases. As explained in Section 3.1, this discrepancy could be attributed to inaccuracies in modelling end correction, whose effect is more pronounced at higher frequencies. Specifically, this could be a

result of the assumption of plane wave propagation within the necks and the cavity components, which is not considered in the FEM. Experimental results also demonstrate consistency in amplitude and peak frequencies, although a more noticeable high-frequency shift is present. As discussed earlier, this is partially due to the exclusion of wall vibration effects in the models. In Appendix B, **Fig. 12** c) and d) present results from FEM accounting for elasticity of the plates. They show that vibration effects contribute to the slight frequency shift, particularly noticeable beyond 2 000 Hz for both profiles. For the ABH profile presented in **Fig. 11** b), more significant differences in the amplitudes of the absorption peaks are apparent between the TMM model and the FEM model, as well as the experimental results. It appears that the TMM model slightly underestimates losses in the material. Given that the zeros of the resonances are positioned below the real frequency axis in the complex frequency plane (see **Fig. 10** d)), an underestimation of losses results in zeros being positioned higher, thus approaching the real frequency axis and leading to higher amplitude absorption peaks.

Note that adjustments were made to the main pore radii to accommodate manufacturing constraints, as not all values were feasible for machining. Consequently, values close to those defined in the previous section were selected (see **Table 1**). That explains the differences between the TMM results shown in **Fig. 11** and those in **Fig. 10**. It can be observed that for the ABH profile with $r_{mp}^{1} = 15$ mm, $r_{mp}^{15} = 1$ mm and $p = 0.8$, the TMM absorption peaks were minimally affected by these adjustments, with amplitudes consistently remaining very close to 1. For the second ABH profile with $r_{mp}^{1} = 11$ mm, $r_{mp}^{15} = 0.75$ mm and $p = 0.5$, the amplitude of the peaks predicted by TMM is more affected, starting from the third absorption peak. Nevertheless, the general behavior remains consistent, with an average absorption band at 0.68 between 1 500 Hz and 4 000 Hz.

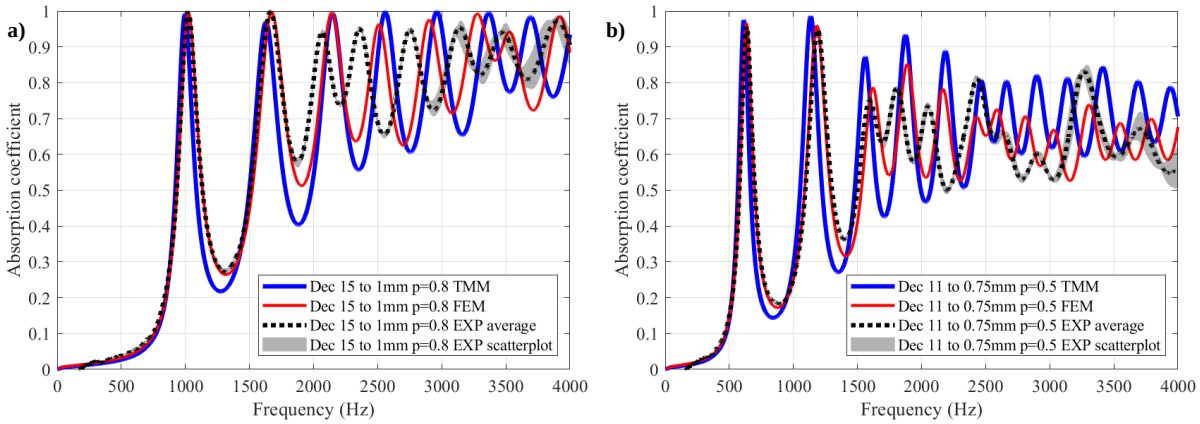


**Fig. 11.** Comparison of the absorption coefficient for the two adapted ABH metamaterial according to the TMM, the FEM and experimental results.

**Table 1.** Main pore radius values for the two broadband ABH profiles

| (mm) | $r_{mp}^{1}$ | $r_{mp}^{2}$ | $r_{mp}^{3}$ | $r_{mp}^{4}$ | $r_{mp}^{5}$ | $r_{mp}^{6}$ | $r_{mp}^{7}$ | $r_{mp}^{8}$ | $r_{mp}^{9}$ | $r_{mp}^{10}$ | $r_{mp}^{11}$ | $r_{mp}^{12}$ | $r_{mp}^{13}$ | $r_{mp}^{14}$ | $r_{mp}^{15}$ |
|---|---|---|---|---|---|---|---|---|---|---|---|---|---|---|---|
| Dec 15-1mm p=0.8 (theoretical 3.5.1) | 15 | 13.30 | 12.05 | 10.92 | 9.86 | 8.86 | 7.89 | 6.96 | 6.05 | 5.17 | 4.30 | 3.46 | 2.62 | 1.81 | 1 |
| Dec 15-1mm p=0.8 (experimental 3.5.2) | 15 | 13 | 12 | 11 | 10 | 9 | 8 | 7 | 6 | 5 | 4.5 | 3.5 | 2.5 | 1.75 | 1 |
| Dec 11-0.75mm p=0.5 (theoretical 3.5.1) | 11 | 8.26 | 7.13 | 6.26 | 5.52 | 4.87 | 4.29 | 3.75 | 3.25 | 2.78 | 2.34 | 1.91 | 1.51 | 1.12 | 0.75 |
| Dec 11-0.75mm p=0.5 (experimental 3.5.2) | 11 | 8.5 | 7 | 6 | 5.5 | 5 | 4.5 | 3.75 | 3.25 | 2.75 | 2.25 | 2 | 1.5 | 1 | 0.75 |



Despite the differences, the absorption curves exhibit consistency, and the comparisons are satisfactory. It is also noteworthy that the experimental curves exhibit a significant improvement in agreement compared to [12]. These results reaffirm the reliability and applicability of the TMM model, thereby further supporting the understanding and conclusions drawn from this analysis.

## 4. Conclusions

The multi-pancake absorber [12] is a thin metamaterial with multiple resonances but relatively narrow absorption peaks, making it suitable for tonal sound attenuation. The variation in the main pore profile of this metamaterial significantly impacts the acoustic absorption. Various profiles were investigated using an adapted TMM, and the results of the modelling were validated through

FEM simulations and measurements in an impedance tube. Analyzing the complex frequency plane representation of the reflection coefficient provided a better understanding of the metamaterial's acoustic response with a constant profile. When the profile is constant, the losses in the different modes are not balanced, resulting in absorption peaks with varying amplitudes. However, by using a decreasing profile of the main pore radius, similar to ABH, we could achieve a better balance of losses between the modes. This results in slightly mistuned local resonances leading to a grouping of the absorption peaks and wider absorption bands. The radius of main pore at the front (the largest) determines the lower boundary of the band gap, while the radius of the main pore at the back (the smallest) intensifies losses in the low frequency modes. Non-linear ABH profiles can be used to further emphasize these losses and equalize the amplitudes of the absorption peaks, if necessary. Thanks to these conclusions, two final ABH profiles were proposed, exhibiting broadband behavior with absorption peaks of similar amplitudes. Compared to the metamaterial with a constant main pore radius, their acoustic absorption is significantly improved, transitioning from spaced peaks with varying amplitudes to a broad absorption band, without increasing the overall thickness. These two profiles also highlight the trade-off between achieving almost perfect absorption peaks and their frequencies.

The metamaterials studied in this work are thin (31 mm), lightweight, non-porous, and provide high sound absorption across a wide frequency range. Additionally, they can be used in harsh environments where conventional porous materials are not suitable. Potential applications include noise reduction in various industries including turbomachinery, rotating machines, aerospace, and industrial settings. However, with an ABH profile an absorption band above 0.7 starts from 1 500 Hz limiting its effectiveness at lower frequencies. The next step involves further improving the structure to enhance the low-frequency wide-band absorption properties. Another interesting

study would be to investigate the behavior of this metamaterial under high sound levels, providing valuable insights into its performance in intense sound environments common in industry. Additionally, it could lead to potential adaptations or optimizations tailored for specific applications.

## CRediT authorship contribution statement

**Gauthier Bezançon:** Conceptualization, Methodology, Formal analysis, Writing – original draft, Visualization. **Olivier Doutres:** Conceptualization, Methodology, Writing – original draft, Supervision. **Olga Umnova:** Methodology, Writing - Review & Editing. **Philippe Leclaire:** Methodology, Writing - Review & Editing. **Thomas Dupont:** Conceptualization, Methodology, Writing – original draft, Supervision.

## Declaration of Competing Interest

None.

## Data Availability

Data will be made available on request.



## Acknowledgements

The authors acknowledge the financial support of Natural Sciences and Engineering Research 545 Council (NSERC) [funding reference numbers: RGPIN-2019-06573].

During the preparation of this work the authors used ChatGPT in order to improve the formulation of some sentences and correct errors. After using this tool, the authors reviewed and edited the content as needed and take full responsibility for the content of the publication.

## Appendix A

The transfer matrix of a cylindrical pore with thickness $h_X$, $T_X(h_X, k_X, Z_X)$, is given by:

$$T_X(h_X, k_X, Z_X) = \begin{bmatrix} \cos(k_X h_X) & jZ_X \sin(k_X h_X) \\ \frac{j}{Z_X} \sin(k_X h_X) & \cos(k_X h_X) \end{bmatrix} \quad (10)$$

The matrices of sudden area discontinuities between a circular section of radius $r_1$ and a circular section of radius $r_2$ is given by:

$$T_{sect,1\to2} = \begin{bmatrix} 1 & 0 \\ 0 & \frac{{r_2}^2}{{r_1}^2} \end{bmatrix} \quad (A.2)$$

## Appendix B

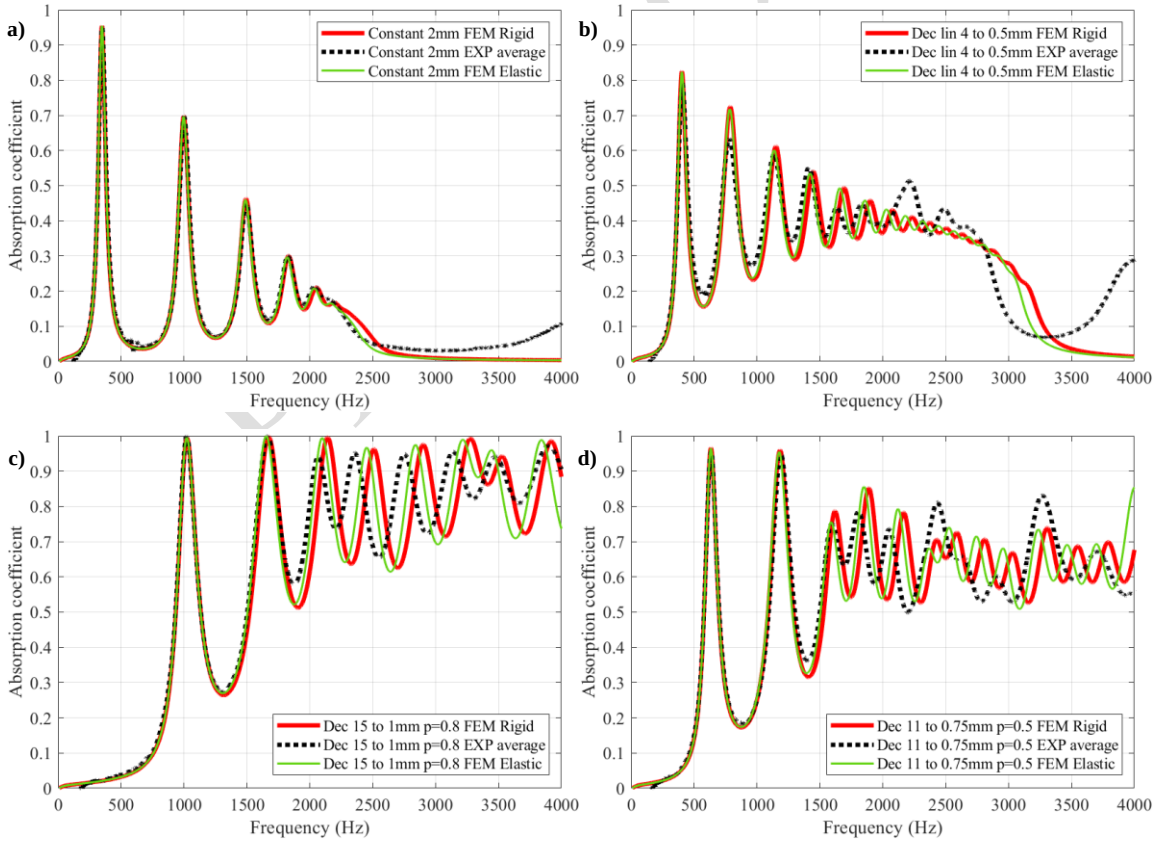


**Fig. 12.** Comparison of the absorption coefficient for metamaterials with a) a constant profile $r_{mp} = 2$ mm, b) a profile decreasing linearly from 4 mm to 0.5 mm and c)-d) the two ABH broadband metamaterials according to FEM Rigid, FEM Elastic and experimental results.

## Appendix C

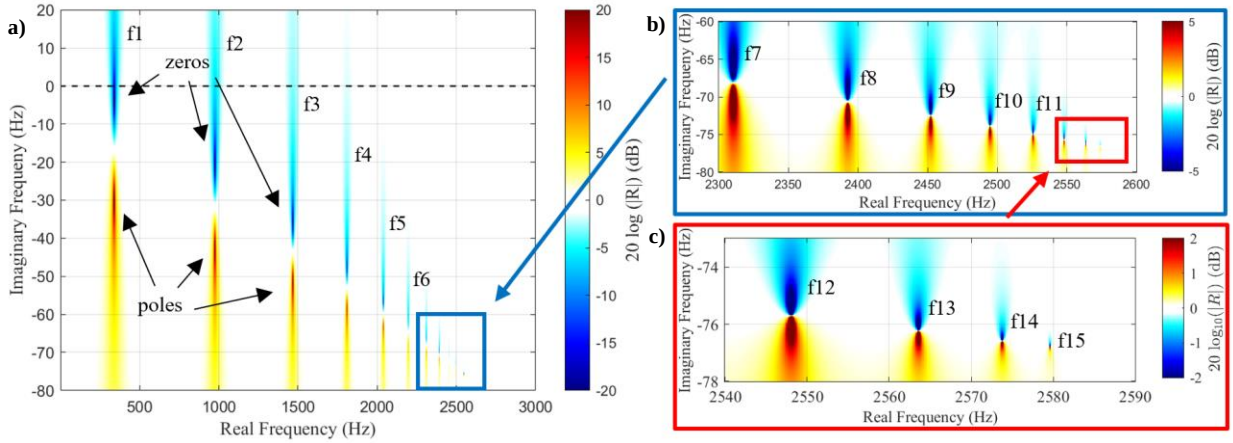


**Fig. 13.** Complex frequency plane representation of 20 log(R) for a metamaterial with a constant main pore radius $r_{mp} = 2$ mm: a) global, b) zoom 1 and c) zoom 2.

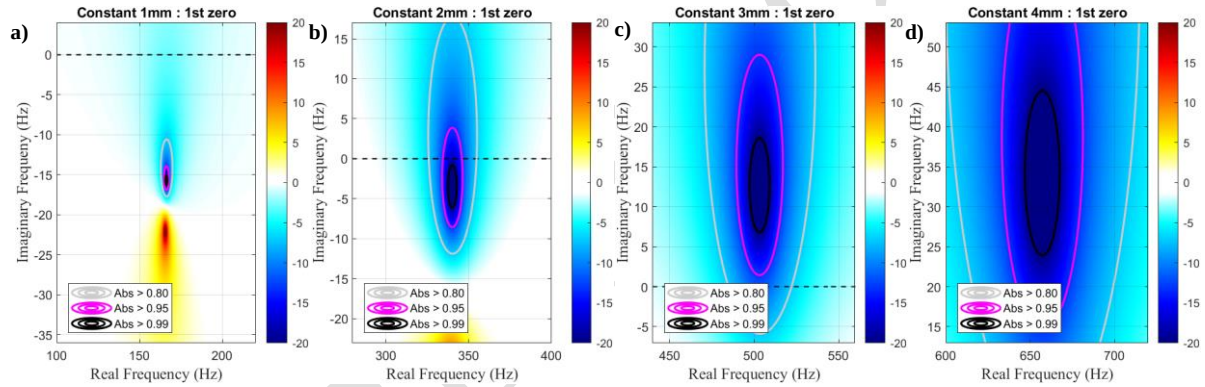


**Fig. 14.** Complex frequency plane representation of 20 log(R) near the first zero for metamaterials with a constant main pore radius: a) $r_{mp} = 1$ mm b) $r_{mp} = 2$ mm c) $r_{mp} = 3$ mm d) $r_{mp} = 4$ mm.

## References


[1] Allard, J.F. and Atalla, N. Propagation of sound in porous media: modelling sound absorbing materials. 2nd ed. New York: John Wiley and Sons; 2009.

[2] Cao, L., Fu, Q., Si, Y., & Yu, J. (2018). Porous materials for sound absorption. Composites Communications, 10, 25–35. https://doi.org/10.1016/j.coco.2018.05.001

[3] Kosten, C. W., & Zwikker, C. (1949). Sound absorbing materials (p. 15). Amsterdam: Elsevier.

[4] Ingard, U. (1953). On the Theory and Design of Acoustic Resonators. Journal of the Acoustical Society of America, 25(6), 1037–1061. https://doi.org/10.1121/1.1907235

[5] Liao, G., Luan, C., Wang, Z., Liu, J., Yao, X., & Fu, J. (2021). Acoustic Metamaterials: A review of theories, structures, fabrication approaches, and applications. Advanced Materials and Technologies, 6(5), 2000787. https://doi.org/10.1002/admt.202000787

[6] Groby, J., Huang, W., Lardeau, A., & Aurégan, Y. (2015). The use of slow waves to design simple sound absorbing materials. Journal of Applied Physics, 117(12), 124903. https://doi.org/10.1063/1.4915115

[7] Jiménez, N., Huang, W., Romero-García, V., Pagneux, V., & Groby, J. (2016). Ultra-thin metamaterial for perfect and quasi-omnidirectional sound absorption. Applied Physics Letters, 109(12). https://doi.org/10.1063/1.4962328

[8] Jiménez, N., Romero-García, V., Pagneux, V., & Groby, J. (2017). Quasiperfect absorption by subwavelength acoustic panels in transmission using accumulation of resonances due to slow sound. Physical Review, 95(1). https://doi.org/10.1103/physrevb.95.014205

[9] Zhang, C., & Hu, X. (2016). Three-Dimensional Single-Port Labyrinthine Acoustic Metamaterial: Perfect Absorption with Large Bandwidth and Tunability. Physical Review Applied, 6(6). https://doi.org/10.1103/physrevapplied.6.064025

[10] Peng, X., Ji, J., & Jing, Y. (2018). Composite honeycomb metasurface panel for broadband sound absorption. Journal of the Acoustical Society of America, 144(4), EL255–EL261. https://doi.org/10.1121/1.5055847

[11] Leclaire, P., Umnova, O., Dupont, T., & Panneton, R. (2015). Acoustical properties of air-saturated porous material with periodically distributed dead-end pores. Journal of the Acoustical Society of America, 137(4), 1772–1782. https://doi.org/10.1121/1.4916712

[12] Dupont, T., Leclaire, P., Panneton, R., & Umnova, O. (2018). A microstructure material design for low frequency sound absorption. Applied Acoustics, 136, 86–93. https://doi.org/10.1016/j.apacoust.2018.02.016

[13] Brooke, D., Umnova, O., Leclaire, P., & Dupont, T. (2020). Acoustic metamaterial for low frequency sound absorption in linear and nonlinear regimes. Journal of Sound and Vibration, 485, 115585. https://doi.org/10.1016/j.jsv.2020.115585

[14] Kone, T. C., Lopez, M., Ghinet, S., Dupont, T., & Panneton, R. (2021). Thermoviscous-acoustic metamaterials to damp acoustic modes in complex shape geometries at low frequencies. Journal of the Acoustical Society of America, 150(3), 2272–2281. https://doi.org/10.1121/10.0006441

[15] Mironov, M. A., & Pislyakov, V. (2002). One-dimensional acoustic waves in retarding structures with propagation velocity tending to zero. Acoustical Physics, 48(3), 347–352. https://doi.org/10.1134/1.1478121

[16] Ouahabi, A. A. E., Krylov, V. V., & O'Boy, D. (2015). Experimental investigation of the acoustic black hole for sound absorption in air. The 22nd International Congress on Sound and Vibration, 2015. Florence, Italy.

[17] Deaconu, M., Radulescu, D., & Vizitiu, G. (2018). Acoustic study of different mufflers based on metamaterials using the black hole principle for aircraft industry. In Conference Proceedings Euronoise (pp. 2271-2275).

[18] Zhang, X., & Li, C. (2021). Broadband and low frequency sound absorption by Sonic black holes with Micro-perforated boundaries. Journal of Sound and Vibration, 512, 116401. https://doi.org/10.1016/j.jsv.2021.116401

[19] Guasch, O., Arnela, M., & Sánchez-Martín, P. (2017). Transfer matrices to characterize linear and quadratic acoustic black holes in duct terminations. Journal of Sound and Vibration, 395, 65–79. https://doi.org/10.1016/j.jsv.2017.02.007

[20] Mironov, M. A., & Pislyakov, V. (2020). One-dimensional sonic black holes: Exact analytical solution and experiments. Journal of Sound and Vibration, 473, 115223. https://doi.org/10.1016/j.jsv.2020.115223

[21] Umnova, O., Brooke, D., Leclaire, P., & Dupont, T. (2023). Multiple resonances in lossy acoustic black holes - theory and experiment. Journal of Sound and Vibration, 543, 117377. https://doi.org/10.1016/j.jsv.2022.117377

[22] Romero-García, V., Theocharis, G., Richoux, O., & Pagneux, V. (2016). Use of complex frequency plane to design broadband and sub-wavelength absorbers. Journal of the Acoustical Society of America, 139(6), 3395–3403. https://doi.org/10.1121/1.4950708

[23] Jiménez, N., Romero-García, V., Pagneux, V., & Groby, J. (2017b). Rainbow-trapping absorbers: Broadband, perfect and asymmetric sound absorption by subwavelength panels for transmission problems. Scientific Reports, 7(1). https://doi.org/10.1038/s41598-017-13706-4

[24] Dickey, N. S., & Selamet, A. (1996). Helmholtz resonators: one-dimensional limit for small cavity length-to-diameter ratios. Journal of Sound and Vibration, 195(3), 512–517. https://doi.org/10.1006/jsvi.1996.0440

[25] ISO 10534-2, Acoustics—Determination of Sound Absorption Coefficient and Impedance in Impedance tubes. Part 2: Transfer-Function Method, International Organization for Standardization, Geneva, Switzerland, 1998.

[26] Dupont, T., Leclaire, P., Sicot, O., Gong, X. L., & Panneton, R. (2011). Acoustic properties of air-saturated porous materials containing dead-end porosity. Journal of Applied Physics, 110(9), 094903. https://doi.org/10.1063/1.3646556.